▮ **Theranostics** │*Very Important Paper*│

Upconverting Carbon Nanodots from Ethylenediaminetetraacetic Acid (EDTA) as Near-Infrared Activated Phototheranostic Agents

M. Carmen Ortega-Liebana,[a, b] M. Mar Encabo-Berzosa,[a, b] Alvaro Casanova,[c] M. Desiree Pereboom,[c] J. Octavio Alda,[c] Jose L. Hueso,*[a, b, d] and Jesus Santamaria*[a, b, d]

Abstract: This work describes the synthesis of nitrogen-doped carbon nanodots (CNDs) synthesized from ethylenediaminetetraacetic acid (EDTA) as a precursor and their application as luminescent agents with a dual-mode theranostic role as near-infrared (NIR) triggered imaging and photodynamic therapy agents. Interestingly, these fluorescent CNDs are more rapidly and selectively internalized by tumor cells and exhibit very limited cytotoxicity until remotely activated with a NIR illumination source. These CNDs are excellent candidates for phototheranostic purposes, for example, simultaneous imaging and therapy can be carried out on cancer cells by using their luminescent properties and the in situ generation of reactive oxidative species (ROS) upon excitation in the NIR range. In the presence of CNDs, NIR remote activation induces the in vitro killing of U251MG cells. Through the use of flow imaging cytometry, we have been able to successfully map and quantify the different types of cell deaths induced by the presence of intracellular superoxide anions ($^\bullet O_2^-$) and hydrogen peroxide (H_2O_2) ROS generated in situ upon NIR irradiation.

Introduction

Phototheranostics has emerged as a novel strategy combining diagnosis and treatment of cancer by using photosensitizing agents that are able to in situ generate reactive oxidative species (ROS) while providing a fluorescent response upon the sole irradiation by an orthogonal stimulus with high spatiotemporal resolution, such as light. The most widespread photodynamic therapy (PDT) agents are porphyrins, phthalocyanines, or bacteriochlorin derivatives co-encapsulated with other fluorescent agents.[1,2] These systems are typically hydrophobic

[a] Dr. M. C. Ortega-Liebana, Dr. M. M. Encabo-Berzosa, Dr. J. L. Hueso, Prof. J. Santamaria
Department of Chemical and Environmental Engineering and
Institute of Nanoscience of Aragon (INA), University of Zaragoza
Campus Rio Ebro, R+D Building, C/Mariano Esquillor s/n
50018, Zaragoza (Spain)
E-mail: jlhueso@unizar.es
        jesus.santamaria@unizar.es

[b] Dr. M. C. Ortega-Liebana, Dr. M. M. Encabo-Berzosa, Dr. J. L. Hueso, Prof. J. Santamaria
Networking Research Center on Bioengineering, Biomaterials and
Nanomedicine (CIBER-BBN), 28029 Madrid (Spain)

[c] Dr. A. Casanova, Dr. M. D. Pereboom, Prof. J. O. Alda
Department of Pharmacology and Physiology
Zaragoza Medical School, University of Zaragoza
C/Domingo Miral s/n, 50009, Zaragoza (Spain)

[d] Dr. J. L. Hueso, Prof. J. Santamaria
Instituto de Ciencia de Materiales de Aragon (ICMA), Consejo Superior de
Investigaciones Científicas (CSIC-Universidad de Zaragoza)
Zaragoza (Spain)

🖳 Supporting information and the ORCID identification number(s) for the
ⓘ author(s) of this article can be found under:
https://doi.org/10.1002/chem.201806307.

and suffer from shallow tissue penetration, limited PDT efficiency, and restricted excitation wavelengths typically located in the blue and red ranges where the penetration depth of light is hindered. To overcome these drawbacks, recent studies have reported the use of alternative nanomaterials such as gold nanomaterials,[1–3] semiconducting quantum dots,[4] semiconducting polymers,[5] sulfide-based nanocrystals,[6] silica nanoparticles,[7] and rare-earth based upconverting inorganic particles.[8–10] These materials have been used as co-photosensitizers (i.e., PDT amplifiers accompanying other sensitizing organic agents) or as light-harvesters in the red and near-infrared (NIR) ranges to favor the deeper penetration of light in the NIR transparent tissue window.[1] Nevertheless, all these alternative sensitizers still face limitations in terms of intrinsic cytotoxicity, colloidal stability, the use of scarce and expensive precursors, or the need for highly complex and time-consuming synthesis and purification protocols.

In this regard, carbon-based nanomaterials such as carbon nanotubes and fullerenes have recently shown high potential as alternative photosensitizers for combined photothermal and photodynamic therapy treatments, which can partially overcome the shortcomings of current NIR phototheranostic agents.[1] Likewise, smaller carbogenic members of the carbon family such as nanodiamonds, polymer nanodots, graphene-like dots, or carbon nanodots (CNDs) have emerged as novel fluorescent nanosensitizers,[11–13] which combine a series of appealing properties such as: 1) high colloidal stability in water and physiological media; 2) high photostability and resistance to photobleaching; 3) reduced toxicity in comparison with nanosystems containing heavy and potentially toxic elements; 4) tunable optical response spanning from UV to NIR ranges including large two-photon excitation cross-sections; 5) abun-

dance of inexpensive precursors for their synthesis; 6) facile and straightforward synthesis protocols. A number of recent studies have successfully reported the use of these carbogenic nanostructures as dual-mode imaging and PDT agents, mostly referred to graphene-like dots or functionalized nanodiamonds.[1,4,14–33] Herein, we report the use of CNDs synthesized by the hydrothermal carbonization (HTC) of ethylenediaminetetraacetic acid (EDTA) at 260 °C (see Experimental Section for further details). This molecular precursor has been selected to induce the direct generation of nitrogen-doped carbon nanodots (N-CNDs) in a single step without the need for secondary amine co-reactants.[34–37] Previous works have claimed that partial substitution of N within the pseudo-graphitic structure of CNDs provides them with an expanded photoluminescence response.[34–42] In this work, we demonstrate that the N-CNDs formed from EDTA exhibit excellent optical photoluminescence (PL) properties in the whole UV/Vis/NIR range. Furthermore, we show their potential as multimodal theranostic agents in the NIR range with simultaneous roles as i) biomarkers that can be readily internalized by tumoral cells and ii) agents capable of in situ generation of highly reactive oxidative species (ROS) after illumination with an NIR source to induce necrosis of the irradiated cells. We also show the potential of flow imaging cytometry to detect in situ the different ROS locally formed upon NIR stimulation of CNDs and the different types of damage and death induced.

Results and Discussion

Synthesis and characterization of EDTA-derived carbon nanodots

The hydrothermal carbonization (HTC) process for the synthesis of the N-CNDs is summarized in Figure 1a. HTC is regarded as a direct and efficient synthetic approach, which works through polymerization and carbonization reactions. It has been widely applied to synthesize a variety of materials owing to the high reactivity of the reactants, easy control of the solution parameters, and limited energy consumption. The process typically proceeds through a number of sequential steps including polymerization and carbonization of organic precursors (Figure 1a). Hu et al.[43] suggested a detailed mechanism proceeding through four stages, including dehydration, polymerization, carbonization, and passivation. They claimed in their study that the molecules assembled as a result of hydrogen bonding. Then, during heating (dehydration), polymerization occurred, leading to a short single burst of nucleation. The resulting nuclei then intergrew by the diffusion of solutes toward the particle surfaces.

Herein, EDTA, a low-cost and naturally abundant amino acid-like compound was utilized as single-source precursor for this purpose. Upon heating, the polymer nanoparticles that begin to form from the initial stage of the EDTA dehydration process shrink as a result of continuous dehydration and C=C and C=N bonds are formed. In parallel, aromatic clusters are formed and when their concentration reaches a critical super-saturation point, nucleation of carbon nanodots takes place after multiple
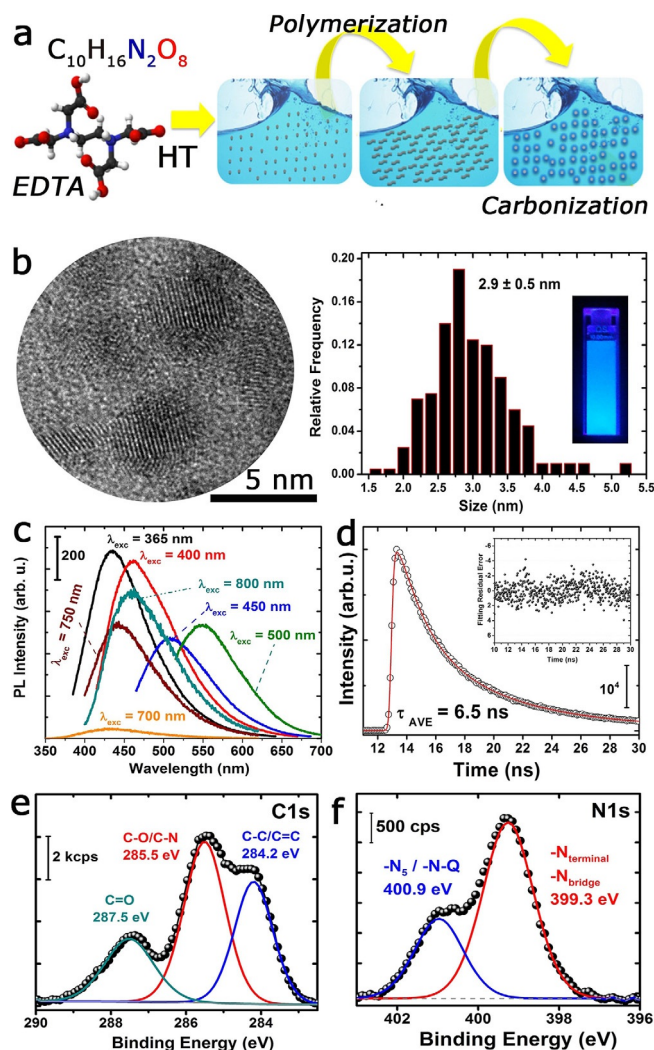
Figure 1. Synthesis and characterization of the N-CNDs. a) Hydrothermal carbonization steps to convert EDTA into N-doped CNDs. b) High-resolution TEM image of the obtained N-CNDs and their corresponding average size distribution (inset: digital image of an aqueous suspension containing N-CNDs and excited by a UV lamp ($\lambda_{exc} = 365$ nm). c) Wavelength-dependent photoluminescence spectra of the N-CNDs. d) Time-resolved fluorescence decay curve of the N-CNDs at an excitation wavelength of 470 nm (inset: residual error after a triple-exponential fitting). e) X-ray photoemission spectrum and fittings corresponding to the C 1s region of the N-CNDs. f) X-ray photoemission spectrum and fittings corresponding to the N 1s region of the N-CNDs.

aggregation events.[43] Finally, the polymers disappear and CNDs remain.[43] TEM analysis shows the presence of crystalline N-CNDs with clear lattice fringes and average sizes of 2.9 ± 0.5 nm (Figure 1b and Figure S1 in the Supporting Information).

Recently, Papaioannou et al.[44] suggested that this crystalline structure can be induced owing to the role of the polymeric units, which act as hot spots during the HT process and the temperature gradients existing in the autoclave. Likewise, these authors postulated that the partial gasification of organic precursors like EDTA under subcritical conditions (in the presence of in situ generated CO/CO_2) leads to the formation of crystalline nuclei through CO_2 reduction under autogenic pres-

sures, which adsorbs onto the surfaces of the hot spots in a sort of chemical vapor deposition (CVD) mechanism.[44] The UV/Vis/NIR absorption spectrum displayed in Figure S2 (in the Supporting Information) reveals maxima at 240 and 360 nm, typically associated with $\pi \rightarrow \pi^*$ (C=C) transitions and $n \rightarrow \pi^*$ (conjugated C—O/C—N) transitions, respectively.[45] Figure 1 c reveals that the N-CNDs exhibit an excitation-dependent emission. As the excitation wavelength increases, the emission spectra progressively redshifts. This typical response arises from the radiative band-edge recombination (electron–hole pair recombination) upon absorption of a photon with energy higher than the band gap energy).

The quantum yields (QYs) corresponding to these samples are close to 17% (see the Experimental Section), which is in good agreement with reports of previous CNDs synthesized under HTC conditions. It is worth mentioning that these N-CNDs also exhibit upconverting behavior (i.e., the emission of photons at higher wavelengths than the excitation wavelength) in the NIR excitation range (750–800 nm). This effect has been attributed to the presence of additional energy π-levels near the LUMO levels of carbon promoted by the N-doped heteroatoms, which facilitate the sequential absorption of less energetic photons that can be re-excited by a second photon to higher unoccupied levels prior to the radiative recombination step.[2, 38, 39, 46–48] This enhanced intramolecular charge transfer efficiency accompanied by an extended light absorption capability across the whole spectrum represents a very attractive optical feature to be exploited in the NIR biological window where the absorption of light by water, tissues, and hemoglobin is minimized. Still, the debate regarding the exact origin of this upconversion mechanism in carbon-based nanoparticles is open and not completely unraveled as additional fluorescent compounds linked to the carbogenic cores may participate in the observed optical response.[38, 49–52] Time-resolved photoluminescence decay measurements fitted well to a sum of three-exponential functions with an average lifetime of 6.5 ns. The shortest fitting components have been previously attributed to intrinsic recombination of populated core states whilst the longer (slower) fitting components are usually related to surface defects, which give rise to surface traps and surface states.[38, 53, 54] The evaluation of the surface functional groups by X-ray photoelectron spectroscopy (XPS) further confirms the enrichment of pyridinic and terminal amines[38, 55, 56] as shown in Figure 1 f for the N 1s region and the major presence of C—O/C—N bonds in the C 1s region (Figure 1 e). Therefore, a carbogenic core enriched on the surface with functional groups containing N heteroatoms seems to be the most plausible configuration for the N-CNDs produced from EDTA by HTC.[38, 56, 57]

## Evaluation as bioimaging agents in the visible/NIR range

The upconversion capabilities of the N-CNDs upon excitation in the NIR range (700–1000 nm) appear especially attractive as the light in this spectral region results in less photo-damage for living organisms and most importantly has a much deeper tissue penetration than visible light. In our work, the N-CNDs were first tested as potential biomarkers in the presence of different cell lines. Confocal images displayed in Figure 2 corroborate that even though N-CND internalization was observed in all cellular types, the uptake from the tumoral cell lines (U251MG and HeLa) was much more relevant at shorter periods of time (4 h and 24 h), especially when lower concentrations of N-CNDs were selected (50 $\mu g\,mL^{-1}$). Previous studies have attributed these differences to the higher negative charge of the surface of cancer cells.[5] The CNDs were preferentially located at the cytoplasm. Three-dimensional histogram images of the cells confirmed the complete internalization. AlamarBlue assays revealed a high biocompatibility of the N-CNDs at the different studied doses and time points, with high U251MG viabilities even for very high concentrations of CNDs (e.g., viability around 80% compared with control (untreated cells), for doses of up to 500 $\mu g\,mL^{-1}$, after 48 h of culture, Figure 2).

The role of these N-CNDs as potential NIR-triggered photodynamic therapeutic agents was evaluated in U251MG cells by using flow cytometry. This technique is extremely sensitive and allows us to monitor cytotoxic responses to photosensitization while simultaneously determining the intracellular production and accumulation of reactive oxidative species (ROS) by using suitable reporting molecules.[58, 59] In particular, the intracellular generation of superoxide anion ($^{\bullet}O_2^{-}$) and hydrogen peroxide (H_2O_2) were detected by using hydroethidine (HE) and dihydrorhodamine 123 (DHR123), respectively[58–60] (see Figure 3 a,b, Experimental Section, and Figures S3–S6 in the Supporting Information). In comparison with control experiments carried out in the absence of N-CNDs, the presence of both reactive species was indicative of intracellular generation of ROS, which increased upon NIR laser irradiation and in a dose-dependent manner regarding the concentration of N-CNDs (Figure 3 a,b). It is noteworthy that the NIR laser irradiation increased the production of both ROS even in the absence of N-CNDs. However, the oxidative stress was much more pronounced upon NIR laser irradiation, with ROS production rates that were more than doubled (for both superoxide anion and hydrogen peroxide) compared with the samples without NIR irradiation.

The detection of these ROS intermediates and others such as singlet oxygen[19] has been previously reported for other carbon-based nanosystems.[14, 20–22, 61–68] The generation of superoxide anions ($^{\bullet}O_2^{-}$) is assisted by the electron donor character of the N-CNDs, which are able to reduce the intracellular O_2 present in the cells[21, 69] (Figure 3 b and Figure S4 in the Supporting Information). Given the high reactivity of this radical, it will rapidly lead to a series of cascade reactions involving the generation of non-radical ROS such as H_2O_2 (Figure 3 a and Figure S4 in the Supporting Information) either through the formation of peroxide intermediates[21] or with the assistance of superoxide dismutases (SOD) activated as ROS scavengers by cells[60] (Figure S4 in the Supporting Information). Hence, N-CNDs can generate additional reactive hydroxyl radicals through the interaction of both species[21] ($^{\bullet}O_2^{-} + H_2O_2 \rightarrow O_2 + {^{\bullet}OH} + OH^{-}$) or by specific redox processes with H_2O or H_2O_2 (Figure S6 in the Supporting Information).[70, 71] Therefore, it is interesting to note that the N-CNDs react preferentially follow-
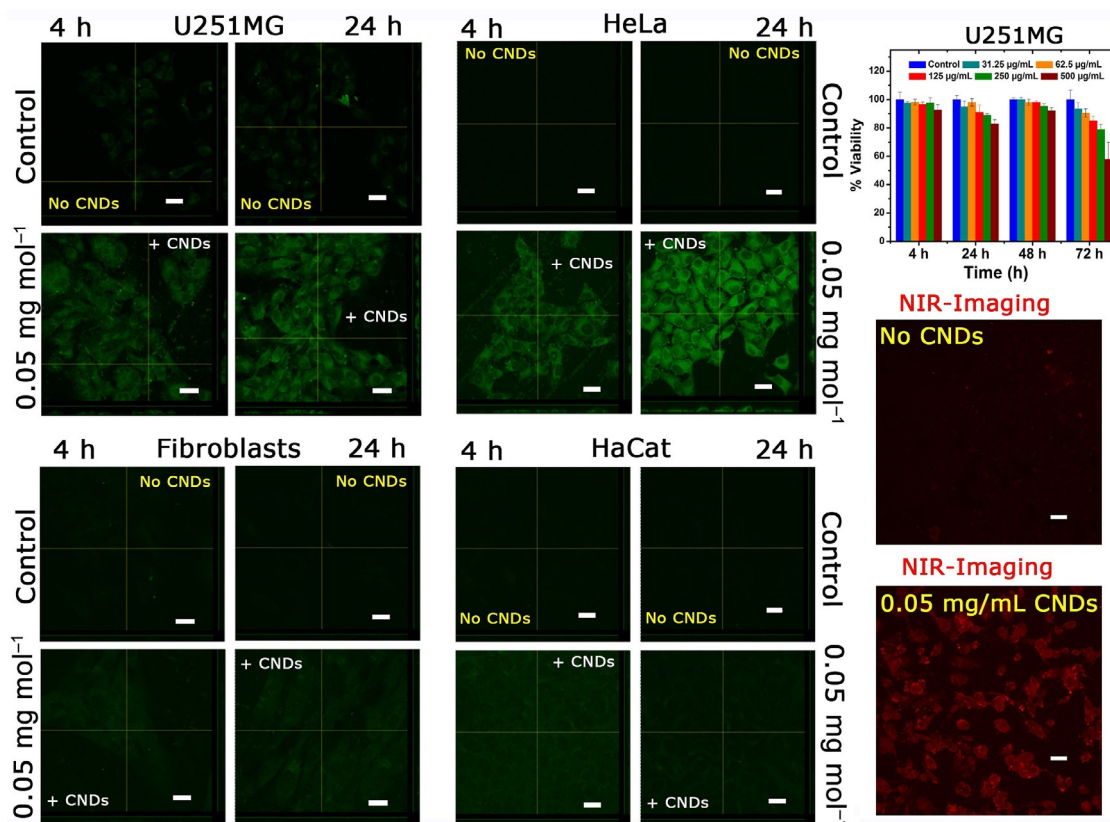
Figure 2. N-CNDs as biomarkers. Confocal images of different cells after 4 h and 24 h of incubation with 0.05 mg mL^{-1} N-CNDs, including three-dimensional histogram images; excitation wavelength: 473 nm. Right top panel corresponds to the evaluation of the cytotoxicity of different N-CND concentrations on U251MG human glioma cells after up to 72 h of internalization and the right bottom images correspond to two-photon imaging of those cells after 24 h incubation and irradiating with a 740 nm excitation wavelength. All scale bars in the confocal images correspond to 20 microns.

ing a PDT type I mechanism typically observed in hypoxic conditions of tumoral cells. NIR light activation promotes an electron transfer mechanism. This performance differs from other organic photosensitizers (i.e., chlorine e6), which require an oxygen-rich atmosphere to generate ROS (PDT type II).[69] Furthermore, flow cytometric analysis by using annexin V-FTIC/propidium iodide (PI) double staining was performed after 10 min NIR laser irradiation of U251MG glioma cells to determine the specific type of cell death induced by the in situ generated ROS (Figure 3 c–e). In contrast to electron spin resonance (EPR) or electrochemical methods, this optical method exhibits several advantages for the in situ monitorization of ROS and permits high-throughput screening and imaging of cells.[58, 68] It was observed that NIR light irradiation of these tumor cells mostly caused necrosis in a short time, and that the proportion of necrotic cells was significantly higher than the others (i.e., apoptotic, etc.). The major changes and damage observed in the cancer cells can be attributed to the disruption induced by ROS, thereby dramatically affecting their permeability and inducing their death. The presence of N-CNDs or the NIR laser irradiation individually resulted in a slight reduction in cell viability, increasing the population of necrotic cells. More specifically, a N-CND dose of 100 µg mL^{-1} produced a smaller necrotic increase than that observed following NIR laser irradiation in the absence of N-CNDs.

The combination of N-CND treatment (100 µg mL^{-1}) and laser irradiation had a synergistic effect, being able to induce necrosis in half of the U251MG population. At higher doses of N-CNDs (400 µg mL^{-1}), the decrease in cell viability can be mainly attributed to the increase in the population of necrotic cells, but also to an increase in early apoptosis, which was not observed with the lower concentration (Figure 3 f). The cell death effects seem to be dose-dependent and increased strongly under 800 nm laser irradiation. Previous works with graphene-like dots claimed an additional photothermal effect as being co-responsible for the photoinduced apoptotic death of tumoral cells caused by locally induced temperature increments.[1, 19, 48] Other N-CNDs required the combined effect of attached specific (chemo)-prodrugs.[1, 22] Instead, the N-CNDs developed in this work act as photosensitizers capable of remote triggering by deeper penetrating NIR light, converting this light into ROS, which cause extensive cell death, (mainly through necrosis) likely caused by a variety of causes: damage to protein, DNA, and lipids, and disruption of the correct functions of mitochondria.[1, 19, 48] In addition, the N-doped CNDs appear to exhibit a successful and preferential internalization in tumoral cells and also play a dual role as NIR responsive biomarkers. All of these characteristics make them highly promising materials in the emerging theranostics field.
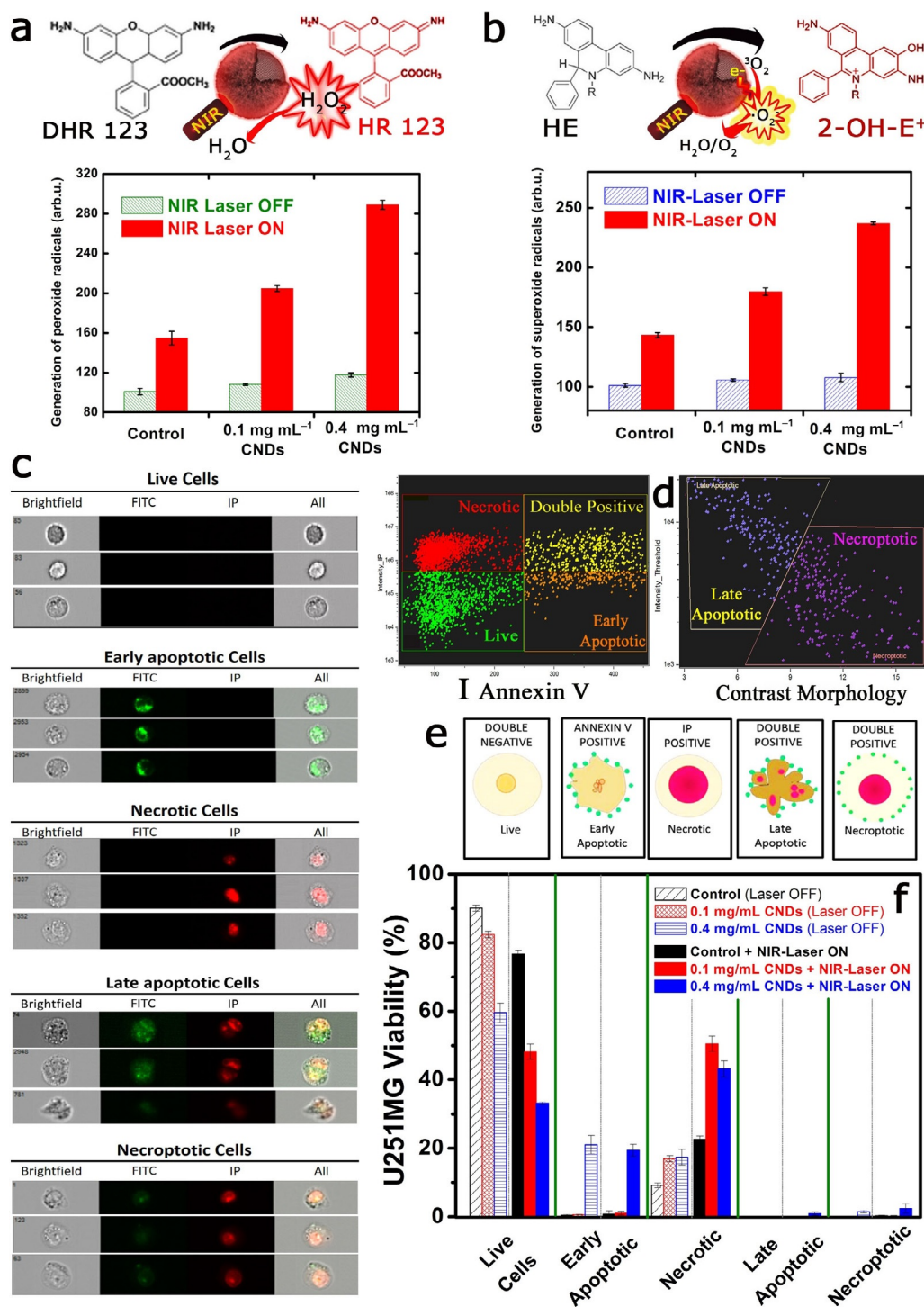
Figure 3. Analysis of N-CNDs as NIR-responsive PDT agents. a) Colorimetric assays carried out to detect the in situ generation of hydrogen peroxide before and after NIR laser irradiation of U251MG cells incubated with different concentrations of N-CNDS, by using DHR 123 as the fluorescent marker. b) Colorimetric detection of superoxide radicals before and after irradiation of U251MG cells incubated with different concentrations of N-CNDS, by using HE as the fluorophore. c) Snapshots of individual U251MG cells acquired by flow cytometry, accounting for the main morphology changes and staining levels acquired depending on the type cell damage. d) Analysis of the different types of cell deaths identified by flow cytometry after 10 min of NIR irradiation of U251MG cells incubated with 0.1 mg mL^{-1} N-CNDs and doubly stained with annexin V and propidium iodide (PI). e) Schematic representation of the change of morphology and staining associated with each specific type of cell death identified in the flow cytometer and depicted in c). f) Cell death analysis identified by flow cytometry for U251MG cells after their incubation with different N-CND concentrations and after being subjected or not to NIR irradiation.

Conclusions

We have synthesized nitrogen-doped carbon dots as photo-enabled theranostic agents. These CNDs were synthesized by hydrothermal carbonization of a single molecular precursor (EDTA) and exhibit an outstanding upconverting response in the near-infrared range, which enabled their simultaneous application as NIR biomarkers with preferential internalization in tumoral cells and their remote NIR activation to efficiently generate ROS to induce cell death. Finally, in this work, flow cytometry has been thoroughly exploited not only to identify the ROS in situ but also to quantify cell death types on a cell to cell basis after illumination with a NIR source.

Experimental Section

Materials

Ethylenediaminetetraacetic acid (EDTA, 99.995%) was obtained from Sigma–Aldrich. All chemicals were of analytical purity grade and were used without further purification. 10 KDa molecular weight cut off (MWCO) membranes (Amicon Ultra-15, Millipore) were also obtained from Sigma–Aldrich.

Synthesis of carbon nanodots

N-doped carbon nanodots (N-CNDs) were easily synthesized in one step by a hydrothermal method. Briefly, 1 M solution of EDTA, as the carbon source, and triple distilled water (10 mL) were mixed in a beaker with a magnetic stirrer, the solution was then transferred into a 25 mL Teflon-lined stainless-steel autoclave and was heated at a constant temperature of 260 °C for 4 h. The resulting solution was cooled to room temperature and was centrifuged at 6000 rpm for 10 min to remove agglomerated particles. The supernatant containing carbon nanomaterials was filtered through a 0.10 mm PTFE membrane (WhatmanTH) membrane to further remove large particles. The brownish yellow supernatant was then dialyzed against ultrapure water through a dialysis membrane for 5 h. This synthesis condition corresponds to the minimum reaction times and temperatures at which CNDs were obtained. Lower T or times failed to give homogeneous and reproducible luminescent nanocarbons with the desired optical response.

Cell culture

The tumoral cell lines U251MG and HeLa cells, and the somatic cell lines (human dermal fibroblast and HaCat keratinocytes) were cultured in Dulbecco's modifies Eagle's medium (DMEM, Gibco) supplemented with 10% fetal bovine serum (FBS, Gibco), 1% penicillin/streptomycin, and 1% amphotericin at 37 °C under a 5% CO$_2$-humidified atmosphere with normoxic conditions. Osteoblasts were cultured in OGM medium (Lonza) under the above-mentioned conditions.

Cytotoxicity evaluation

The in vitro cytotoxicity of the N-CNDs was determined by using the AlamarBlue assay. For that, U251MG cells were seeded onto a 96-well microplate at a density of 5×10^3 cells per well and cultured for 24 h. After that, the culture medium was removed and the cells were treated with 100 µL of different N-CND solutions in DMEM (31.25 µg mL^{-1} to 1 mg mL^{-1} (serial dilutions)) and were cultured

for another 4, 24, 48, and 72 h. Cells without exposure to N-CNDs were used as the control. At the selected incubation times, treatments were removed and U251MG cells were washed twice with PBS, following by the addition of DMEM containing 10% (v/v) AlamarBlue. Culture plates were maintained under normoxic conditions in a 5% CO$_2$ incubator at 37 °C for 3 h. Afterwards, fluorescence changes were evaluated at 530/590 nm excitation/emission wavelengths by using a Synergy HT (Biotek).

Bioimaging confocal experiments

The internalization and in vitro emission of N-CNDs was evaluated in different cell types at two different incubation times (4 and 24 h) and two concentrations (50 and 400 µg mL^{-1}). The N-CND solutions used in the assays were obtained by diluting the stock solutions in culture cell medium. The final concentration of water in the final medium employed did not cause any osmotic imbalance. First, different cells types were cultured as mentioned above. Briefly, cells were seeded on sterile cover-slips at a density of 40 000 cells per well and were incubated for 24 h to facilitate substrate adhesion. After that, the medium was removed and N-CND suspensions were added to the cultured cells. At the incubation times selected (4 and 24 h), the medium containing N-CNDs was removed and cells were washed twice with PBS, to eliminate non-internalized nanoparticles, and fixed with 4% paraformaldehyde. Subsequently, the cover-slips were mounted and the samples were observed in an Olympus FV10-i Oil Type confocal microscopy with a laser excitation source at 473 nm and analyzed with the microscopy software. Analogous settings were employed for both the control experiments (without N-CNDs) and the treated samples.

Oxidative stress determination

The intracellular general ROS production was detected by the oxidation-sensitive fluorescent probe dyes. Specifically, hydrogen peroxide production was measured by using dihydrorhodamine 123 (DHR, Sigma–Aldrich) and superoxide anion formation was studied by using hydroethidine (HE, Sigma–Aldrich). It is important to remark that ROS production measurement was carried out in live cells, which were stained with propidium iodide (0.025 mM, Sigma–Aldrich) incubation for 15 min. After that, individual fluorescence cell intensity was analyzed by using an ImageStreamX image cytometer (Amnis, Seattle, WA), measuring the emission between 520–617 nm under an excitation wavelength of 488 nm. Briefly, U251MG were seeded onto 48-well microplates and incubated with N-CNDs at two different concentrations (100 and 400 µg mL^{-1}) for 24 h. After that, cells were irradiated for 10 min by using a NIR laser (808 nm, 2 W cm^{-2}). Subsequently, cells were stained with DHR123 or HE, and cellular fluorescence intensity was analyzed with an ImageStreamX image cytometer, measuring the fluorescence emission at 480–560 nm (DHR) or 595–660 nm (HE) under 488 nm excitation. Cells without nanoparticles and non-irradiated were used as the control. The effect of N-CNDs without laser irradiation and laser irradiation without N-CND incubation was also evaluated.

Cell death analysis

The cell death study was based on cells' morphological analysis by using double labeling with annexin V and propidium iodide (AV/IP), which allows us to divide cells into four populations: live cells (negative for both dyes), necrotic (AV−, IP+), early apoptotic (AV+, IP−), and late apoptotic/necroptotic cells (positive for both dyes). In summary, cells were incubated with the N-CNDs at the

concentrations of 100 and 400 µg mL^{-1} and subsequently irradiated with a NIR laser (808 nm, 2 W cm^{-2}) coupled to a fiber collimator (THORLABS F220SMA-780, 780 nm, $f = 11.07$ mm) for 10 min. Cells without nanoparticles and those not irradiated were used as controls. Also, the effects of N-CNDs without laser irradiation and laser effect without N-CND incubation were studied. Cytometer results were analyzed by using the IDEAS software, which allows the differentiation between late apoptotic and necroptotic populations through "Contrast_Morphology vs. Intensity_Threshold" morpho-cytometric parameters separation.

Statistical analysis

All the experiments were repeated at least six times as independent experiments. The results are represented as mean $+/-$ standard deviation. The normal distribution was tested by the Kolmogorov–Smirnov test; statistical significance was set at $p < 0.05$. For the parametric data, a multiple comparison was made with ANOVA followed by a comparison of two by two with the t-test. For no parametric data, Kruskal–Wallis was performed followed by the U Mann Whitney comparison test.

Characterization techniques

The morphologies and particle size distributions were determined by transmission electron microscopy (TEM; FEI Tecnai T20 and F30, operated at 200 and 300 kV, respectively). To prepare the samples, the nanoparticle suspensions were diluted with water prior to casting on a holey carbon TEM grid. The functionalization of the CND surface was analyzed by X-ray photoelectron spectroscopy (XPS) with an Axis Ultra DLD (Kratos Tech.). A monochromatic Al$_{K\alpha}$ source (1486.6 eV) was employed with multiple runs at 12 kV, 10 mA, and pass energy of 20 eV. The binding energies were calibrated to the internal C 1s (284.3 eV) standard. Analyses of the peaks were performed with CasaXPS software, by using a weighted sum of Lorentzian and Gaussian component curves after Shirley background subtraction. Steady-state fluorescence emission spectra were collected with a JASCO FP-6500 spectrofluorometer equipped with a 450 W xenon lamp for excitation, with temperature controller ETC-273T at 25 °C, using 5×10 mm cuvettes, and a LS55 Fluorescence Spectrometer (PerkinElmer) equipped with a xenon arc lamp as the light source and a quartz cell (10×10 mm). The excitation wavelengths used in the experiments to record the emission spectra were 400 and 740 nm. Both excitation and emission slits were 3 nm.

The fluorescence quantum yields ϕ of the different CNDs in aqueous solution were computed according to Equation (1):

$$\phi_S = \phi_R \times F_S \times (1 - 10^{-A_R(\lambda_{exc})}) \times n_S^2)/F_R \times (1 - 10^{-A_S(\lambda_{exc})}) \times n_R^2) \tag{1}$$

The subscript S refers to the CND samples, R stands for the selected reference fluorophore (quinine sulfate, 0.1 M H$_2$SO$_4$) with known quantum yield (0.54), F stands for the corrected, integrated fluorescence spectra, $A(\lambda_{exc})$ denotes the absorbance at the used excitation wavelength λ_{exc}, and n represents the refractive index of the solvent. To minimize inner filter effects, the absorbance at the excitation wavelength λ_{exc} was kept under 0.1. The measurements were performed by using 10 mm optical path length cuvettes under right-angle (L) arrangement and "magic angle" conditions. The averages and standard uncertainties of ϕ are computed from independent ϕ measurements (2 conc. of sample×2 conc. of reference×2 excitation wavelengths λ_{exc}). Fluorescence decay traces of the different CNDs were recorded in the time-correlated single-photon counting (TCSPC) mode by using the FluoTime 200 fluorometer (PicoQuant, GmbH). Briefly, the samples were excited by a 405 nm picosecond pulsed diode laser (Edinburgh EPL405) with a 10 MHz repetition rate. The full width at half maximum of the laser pulse was approximately 90 ps. The fluorescence was collected after passing through a polarizer set at the magic angle, and a 2 nm bandwidth monochromator. Fluorescence decay histograms were collected by using a TimeHarp200 board, with a time increment per channel of 36 ps, at the emission wavelengths of 450, 460, and 470 nm. The histograms of the instrument response function (IRF) were determined by using a LUDOX scatterer, and sample decays were recorded until they typically reached 2×10^4 counts in the peak channel, as it is well known that complex decays can be well described by the simplest exponential models if the fitting is carried out from experimental data with a low number of CPC.

Conflict of interest

The authors declare no conflict of interest.

[1] K. R. Deng, C. X. Li, S. S. Huang, B. G. Xing, D. Y. Jin, Q. G. Zeng, Z. Y. Hou, J. Lin, *Small* **2017**, *13*, 1702299.

[2] J. Croissant, A. Chaix, O. Mongin, M. Wang, S. Clement, L. Raehm, J. O. Durand, V. Hugues, M. Blanchard-Desce, M. Maynadier, A. Gallud, M. Gary-Bobo, M. Garcia, J. Lu, F. Tamanoi, D. P. Ferris, D. Tarn, J. I. Zink, *Small* **2014**, *10*, 1752–1755.

[3] D. Yang, G. X. Yang, P. P. Yang, R. C. Lv, S. L. Gai, C. X. Li, F. He, J. Lin, *Adv. Funct. Mater.* **2017**, *27*, 1700371.

[4] H. Y. Huang, J. F. Lovell, *Adv. Funct. Mater.* **2017**, *27*, 1603524.

[5] D. Wang, H. F. Su, R. T. K. Kwok, X. L. Hu, H. Zou, Q. X. Luo, M. M. S. Lee, W. H. Xu, J. W. Y. Lam, B. Tang, *Chem. Sci.* **2018**, *9*, 3685–3693.

[6] I. O. de Solorzano, M. Prieto, G. Mendoza, T. Alejo, S. Irusta, V. Sebastian, M. Arruebo, *ACS Appl. Mater. Interfaces* **2016**, *8*, 21545–21554.

[7] M. Gary-Bobo, Y. Mir, C. Rouxel, D. Brevet, I. Basile, M. Maynadier, O. Vaillant, O. Mongin, M. Blanchard-Desce, A. Morere, M. Garcia, J. O. Durand, L. Raehm, *Angew. Chem. Int. Ed.* **2011**, *50*, 11425–11429; *Angew. Chem.* **2011**, *123*, 11627–11631.

[8] Z. J. Gu, L. Yan, G. Tian, S. J. Li, Z. F. Chai, Y. L. Zhao, *Adv. Mater.* **2013**, *25*, 3758–3779.

[9] L. L. Feng, S. L. Gai, F. He, Y. L. Dai, C. N. Zhong, P. P. Yang, J. Lin, *Biomaterials* **2017**, *147*, 39 – 52.

[10] L. L. Feng, F. He, B. Liu, G. X. Yang, S. L. Gai, P. P. Yang, C. X. Li, Y. L. Dai, R. C. Lv, J. Lin, *Chem. Mater.* **2016**, *28*, 7935 – 7946.

[11] T. Gao, X. Wang, L. Y. Yang, H. He, X. X. Ba, J. Zhao, F. L. Jiang, Y. Liu, *ACS Appl. Mater. Interfaces* **2017**, *9*, 24846 – 24856.

[12] Z. Q. Xu, J. Y. Lan, J. C. Jin, P. Dong, F. L. Jiang, Y. Liu, *ACS Appl. Mater. Interfaces* **2015**, *7*, 28346 – 28352.

[13] Z. Q. Xu, L. Y. Yang, X. Y. Fan, J. C. Jin, J. Mei, W. Peng, F. L. Jiang, Q. Xiao, Y. Liu, *Carbon* **2014**, *66*, 351 – 360.

[14] M. Nurunnabi, Z. Khatun, G. R. Reeck, D. Y. Lee, Y. K. Lee, *ACS Appl. Mater. Interfaces* **2014**, *6*, 12413 – 12421.

[15] M. Kim, J. Jang, C. Cha, *Drug Discovery Today* **2017**, *22*, 1430 – 1437.

[16] H. Huang, C. G. Li, S. J. Zhu, H. L. Wang, C. L. Chen, Z. R. Wang, T. Y. Bai, Z. Shi, S. H. Feng, *Langmuir* **2014**, *30*, 13542 – 13548.

[17] K. Albert, H. Y. Hsu, *Molecules* **2016**, *21*, 1585.

[18] Z. Khatun, M. Nurunnabi, M. Nafiujjaman, G. R. Reeck, H. A. Khan, K. J. Cho, Y. K. Lee, *Nanoscale* **2015**, *7*, 10680 – 10689.

[19] J. C. Ge, M. H. Lan, B. J. Zhou, W. M. Liu, L. Guo, H. Wang, Q. Y. Jia, G. L. Niu, X. Huang, H. Y. Zhou, X. M. Meng, P. F. Wang, C. S. Lee, W. J. Zhang, X. D. Han, *Nat. Commun.* **2014**, *5*, 4596.

[20] M. Zhang, W. T. Wang, N. L. Zhou, P. Yuan, Y. T. Su, M. N. Shao, C. Chi, F. Y. Pan, *Carbon* **2017**, *118*, 752 – 764.

[21] X. N. Dou, Z. Lin, H. Chen, Y. Z. Zheng, C. Lu, J. M. Lin, *Chem. Commun.* **2013**, *49*, 5871 – 5873.

[22] Y. L. Pang, Z. H. Mai, B. Wang, L. Wang, L. P. Wu, X. P. Wang, T. S. Chen, *Oncotarget* **2017**, *8*, 93800 – 93812.

[23] Y. Choi, S. Kim, M. H. Choi, S. R. Ryoo, J. Park, D. H. Min, B. S. Kim, *Adv. Funct. Mater.* **2014**, *24*, 5781 – 5789.

[24] P. Huang, J. Lin, X. S. Wang, Z. Wang, C. L. Zhang, M. He, K. Wang, F. Chen, Z. M. Li, G. X. Shen, D. X. Cui, X. Y. Chen, *Adv. Mater.* **2012**, *24*, 5104 – 5110.

[25] S. Y. Lim, W. Shen, Z. Q. Gao, *Chem. Soc. Rev.* **2015**, *44*, 362 – 381.

[26] K. Yang, L. Z. Feng, X. Z. Shi, Z. Liu, *Chem. Soc. Rev.* **2013**, *42*, 530 – 547.

[27] J. C. Ge, Q. Y. Jia, W. M. Liu, M. H. Lan, B. J. Zhou, L. Guo, H. Y. Zhou, H. Y. Zhang, Y. Wang, Y. Gu, X. M. Meng, P. F. Wang, *Adv. Healthcare Mater.* **2016**, *5*, 665 – 675.

[28] B. J. Geng, D. W. Yang, D. Y. Pan, L. Wang, F. F. Zheng, W. W. Shen, C. Zhang, X. K. Li, *Carbon* **2018**, *134*, 153 – 162.

[29] P. W. Gong, L. Sun, F. Wang, X. C. Liu, Z. Q. Yan, M. Z. Wang, L. Zhang, Z. Z. Tian, Z. Liu, J. M. You, *Chem. Eng. J.* **2019**, *356*, 994 – 1002.

[30] X. Bao, Y. Yuan, J. Q. Chen, B. H. Zhang, D. Li, D. Zhou, P. T. Jing, G. Y. Xu, Y. L. Wang, K. Hola, D. Z. Shen, C. F. Wu, L. Song, C. B. Liu, R. Zboril, S. N. Qu, *Light: Sci. Appl.* **2018**, *7*, 91.

[31] M. H. Lan, S. J. Zhao, Z. Y. Zhang, L. Yan, L. Guo, G. L. Niu, J. F. Zhang, J. F. Zhao, H. Y. Zhang, P. F. Wang, G. Y. Zhu, C. S. Lee, W. J. Zhang, *Nano Res.* **2017**, *10*, 3113 – 3123.

[32] Q. Y. Jia, J. C. Ge, W. M. Liu, S. Liu, G. L. Niu, L. Guo, H. Y. Zhang, P. F. Wang, *Nanoscale* **2016**, *8*, 13067 – 13077.

[33] L. J. Luo, C. Liu, T. He, L. Y. Zeng, J. Xing, Y. Z. Xia, Y. W. Pan, C. Y. Gong, A. G. Wu, *Nanoscale* **2018**, *10*, 22035 – 22043.

[34] D. Y. Pan, J. C. Zhang, Z. Li, C. Wu, X. M. Yan, M. H. Wu, *Chem. Commun.* **2010**, *46*, 3681 – 3683.

[35] D. Y. Pan, J. C. Zhang, Z. Li, Z. W. Zhang, L. Guo, M. H. Wu, *J. Mater. Chem.* **2011**, *21*, 3565 – 3567.

[36] Y. H. Deng, X. Chen, F. Wang, X. A. Zhang, D. X. Zhao, D. Z. Shen, *Nanoscale* **2014**, *6*, 10388 – 10393.

[37] Y. J. Zhang, R. R. Yuan, M. L. He, G. C. Hu, J. T. Jiang, T. Xu, L. Zhou, W. Chen, W. D. Xiang, X. J. Liang, *Nanoscale* **2017**, *9*, 17849 – 17858.

[38] M. C. Ortega-Liebana, M. M. Encabo-Berzosa, M. J. Ruedas-Rama, J. L. Hueso, *Chem. Eur. J.* **2017**, *23*, 3067 – 3073.

[39] B. Kong, A. W. Zhu, C. Q. Ding, X. M. Zhao, B. Li, Y. Tian, *Adv. Mater.* **2012**, *24*, 5844 – 5848.

[40] H. Tetsuka, R. Asahi, A. Nagoya, K. Okamoto, I. Tajima, R. Ohta, A. Okamoto, *Adv. Mater.* **2012**, *24*, 5333 – 5338.

[41] Y. Q. Dong, H. C. Pang, H. B. Yang, C. X. Guo, J. W. Shao, Y. W. Chi, C. M. Li, T. Yu, *Angew. Chem. Int. Ed.* **2013**, *52*, 7800 – 7804; *Angew. Chem.* **2013**, *125*, 7954 – 7958.

[42] S. L. Hu, A. Trinchi, P. Atkin, I. Cole, *Angew. Chem. Int. Ed.* **2015**, *54*, 2970 – 2974; *Angew. Chem.* **2015**, *127*, 3013 – 3017.

[43] Y. P. Hu, J. Yang, J. W. Tian, J. S. Yu, *J. Mater. Chem. B* **2015**, *3*, 5608 – 5614.

[44] N. Papaioannou, A. Marinovic, N. Yoshizawa, A. E. Goode, M. Fay, A. Khlobystoyv, M. M. Titirici, A. Sapelkin, *Sci. Rep.* **2018**, *8*, 6559.

[45] D. Qu, M. Zheng, J. Li, Z. G. Xie, Z. C. Sun, *Light: Sci. Appl.* **2015**, *4*, e364.

[46] A. Gulzar, J. T. Xu, P. P. Yang, F. He, L. G. Xu, *Nanoscale* **2017**, *9*, 12248 – 12282.

[47] Y. Huang, F. Qiu, L. Y. Shen, D. Chen, Y. Su, C. Yang, B. Li, D. Y. Yan, X. Y. Zhu, *ACS Nano* **2016**, *10*, 10489 – 10499.

[48] S. Y. Lu, L. Z. Sui, J. J. Liu, S. J. Zhu, A. M. Chen, M. X. Jin, B. Yang, *Adv. Mater.* **2017**, *29*, 1603443.

[49] J. B. Essner, J. A. Kist, L. Polo-Parada, G. A. Baker, *Chem. Mater.* **2018**, *30*, 1878 – 1887.

[50] J. Schneider, C. J. Reckmeier, Y. Xiong, M. von Seckendorff, A. S. Susha, P. Kasak, A. L. Rogach, *J. Phys. Chem. C* **2017**, *121*, 2014 – 2022.

[51] S. J. Zhu, X. H. Zhao, Y. B. Song, S. Y. Lu, B. Yang, *Nano Today* **2016**, *11*, 128 – 132.

[52] L. Shi, J. H. Yang, H. B. Zeng, Y. M. Chen, S. C. Yang, C. Wu, H. Zeng, O. Yoshihito, Q. Q. Zhang, *Nanoscale* **2016**, *8*, 14374 – 14378.

[53] A. Orte, J. M. Alvarez-Pez, M. J. Ruedas-Rama, *ACS Nano* **2013**, *7*, 6387 – 6395.

[54] M. J. Ruedas-Rama, J. D. Walters, A. Orte, E. A. H. Hall, *Anal. Chim. Acta* **2012**, *751*, 1 – 23.

[55] M. C. Ortega-Liebana, J. L. Hueso, S. Ferdousi, R. Arenal, S. Irusta, K. L. Yeung, J. Santamaria, *Appl. Catal. B* **2017**, *218*, 68 – 79.

[56] J. L. Hueso, J. P. Espinos, A. Caballero, J. Cotrino, A. R. Gonzalez-Elipe, *Carbon* **2007**, *45*, 89 – 96.

[57] M. C. Ortega-Liebana, N. X. Chung, R. Limpens, L. Gomez, J. L. Hueso, J. Santamaria, T. Gregorkiewicz, *Carbon* **2017**, *117*, 437 – 446.

[58] M. J. Naya, D. Pereboom, J. Ortego, J. O. Alda, A. Lanas, *Gut* **1997**, *40*, 175 – 181.

[59] Y. Gilaberte, D. Pereboom, F. J. Carapeto, J. O. Alda, *Photodermatol. Photoimmunol. Photomed.* **1997**, *13*, 43 – 49.

[60] H. T. Zhao, S. Kalivendi, H. Zhang, J. Joseph, K. Nithipatikom, J. Vasquez-Vivar, B. Kalyanaraman, *Free Radical Biol. Med.* **2003**, *34*, 1359 – 1368.

[61] Z. M. Markovic, B. Z. Ristic, K. M. Arsikin, D. G. Klisic, L. M. Harhaji-Trajkovic, B. M. Todorovic-Markovic, D. P. Kepic, T. K. Kravic-Stevovic, S. P. Jovanovic, M. M. Milenkovic, D. D. Milivojevic, V. Z. Bumbasirevic, M. D. Dramicanin, V. S. Trajkovic, *Biomaterials* **2012**, *33*, 7084 – 7092.

[62] D. Q. Chen, C. A. Dougherty, K. C. Zhu, H. Hong, *J. Controlled Release* **2015**, *210*, 230 – 245.

[63] T. K. Ryu, S. W. Baek, R. H. Kang, K. Y. Jeong, D. R. Jun, S. W. Choi, *J. Controlled Release* **2018**, *270*, 237 – 245.

[64] H. T. Li, Z. H. Kang, Y. Liu, S. T. Lee, *J. Mater. Chem.* **2012**, *22*, 24230 – 24253.

[65] X. D. Xu, P. E. Saw, W. Tao, Y. J. Li, X. Y. Ji, S. Bhasin, Y. L. Liu, D. Ayyash, J. Rasmussen, M. Huo, J. J. Shi, O. C. Farokhzad, *Adv. Mater.* **2017**, *29*, 1700141.

[66] P. C. Hsu, P. C. Chen, C. M. Ou, H. Y. Chang, H. T. Chang, *J. Mater. Chem. B* **2013**, *1*, 1774 – 1781.

[67] C. L. Li, C. M. Ou, C. C. Huang, W. C. Wu, Y. P. Chen, T. E. Lin, L. C. Ho, C. W. Wang, C. C. Shih, H. C. Zhou, Y. C. Lee, W. F. Tzeng, T. J. Chiou, S. T. Chu, J. Cang, H. T. Chang, *J. Mater. Chem. B* **2014**, *2*, 4564 – 4571.

[68] F. Si, Y. Liu, K. L. Yan, W. W. Zhong, *Chem. Commun.* **2015**, *51*, 7931 – 7934.

[69] Z. J. Zhou, J. B. Song, L. M. Nie, X. Y. Chen, *Chem. Soc. Rev.* **2016**, *45*, 6597 – 6626.

[70] M. C. Ortega-Liebana, J. L. Hueso, S. Ferdousi, K. L. Yeung, J. Santamaria, *Diam. Relat. Mater.* **2016**, *65*, 176 – 182.

[71] M. C. Ortega-Liebana, J. L. Hueso, A. Larrea, V. Sebastiana, J. Santamaria, *Chem. Commun.* **2015**, *51*, 16625 – 16628.